

# The pressure disturbance of a nonlinear internal wave train

By J. N. MOUM AND W. D. SMYTH

College of Oceanic & Atmospheric Sciences, Oregon State University,  
104 COAS Admin. Bldg, Corvallis, OR 97331-5503, USA

(Received 14 July 2005 and in revised form 4 December 2005)

Observations from a lander fixed to the seafloor over the continental shelf in 124 m of water provide highly resolved velocity measurements through nonlinear internal waves of elevation. From these measurements we determine, for the first time, the non-hydrostatic pressure disturbance ( $p_{nh}$ ) in nonlinear internal waves. For near-bottom waves of elevation ranging in amplitude,  $a$ , from 12 to 33 m, the value of  $p_{nh}$  evaluated at the seafloor changes sign from  $> 0$  to  $< 0$  and back in accordance with weakly nonlinear theory; peak values of  $|p_{nh}|$  range from 25 to 90 N m<sup>-2</sup>. The external hydrostatic pressure disturbance due to the surface displacement ( $\eta_H$ ) is inferred from horizontal accelerations. For elevation waves,  $\eta_H < 0$ ; peak values range from 0.1 to 9 mm (1 to 90 N m<sup>-2</sup>). The internal hydrostatic pressure perturbation ( $p_{wh}$ ), caused by isopycnal displacement, is inferred from measured streamlines and an ambient density profile. Its value at the seafloor is  $> 0$  for elevation waves; peak values range from 100 to 300 N m<sup>-2</sup>.  $|\eta_H|$  and seafloor values of  $|p_{nh}|$ ,  $p_{wh}$  all increase monotonically with  $a$ . Since  $|p_{nh}|$  and  $p_{wh}$  increase at roughly the same rate with  $a$ , no clear trend arises in the degree to which waves become more or less non-hydrostatic as  $a$  changes.

A distinct bottom pressure signature is determined for bottom-trapped nonlinear waves of elevation, a wave train consisting of a sequence of positive pressure perturbations (dominated by  $p_{wh}$ ). By inference, a train of surface-trapped nonlinear internal waves of depression will consist of a sequence of negative pressure perturbations. A result of this analysis is that significant properties of the waves can be discerned from a simple adequately resolved bottom pressure measurement.

---

## 1. Introduction

Where near-surface pycnoclines exist in the coastal ocean, large-amplitude nonlinear solitary-like internal waves are commonly found (Apel *et al.* 1985; Moum *et al.* 2003). These near-surface waves depress the pycnocline and hence are referred to as waves of depression. Their surface signature is detectable by satellite-borne synthetic aperture radar (SAR) as bands of alternating high and low radar reflectivity. Their ubiquitous presence in SAR imagery (Fu & Holt 1982) has generated considerable interest in their effect on acoustic propagation, their role in tidal energy dissipation and their interactions with local biochemical signals. Where near-bottom pycnoclines exist, it appears that high-amplitude nonlinear solitary-like internal waves of elevation are also common (Bogucki, Dickey & Redekopp 1997; Hosegood & van Haren 2003; Klymak & Moum 2003), although their surface signature is considerably weaker than that of depression waves; in fact, such waves are generally not detectable by their surface signatures. These waves have much in common with atmospheric phenomena

such as the ‘Morning Glory’ observed in northern Australia (Christie, Muirhead & Clarke 1981; Clarke, Smith & Reid 1981), which in turn have been the focus of laboratory (Rottman & Simpson 1989) and theoretical (Horn *et al.* 2000) studies.

Observations of nonlinear internal waves include SAR, which defines the waves’ surface structure over scales of  $O(100\text{ km})$ , and acoustic backscatter (Moum *et al.* 2003), velocity and density profile measurements (Apel *et al.* 1995), all of which can define the waves’ internal structure either in time or in space. There is also a measurable bottom pressure signature which has not previously been quantified. This consists of three components: an external hydrostatic pressure perturbation due to deflection of the free surface caused by velocity convergence/divergence there, an internal hydrostatic pressure perturbation due to the displacement of isopycnals, and a non-hydrostatic pressure perturbation caused by vertical fluid accelerations.

This paper describes *in situ* observations of large-amplitude waves of elevation over the continental shelf off Oregon. We first define the pressure disturbance of nonlinear internal waves (§2.1) and discuss the structure of the disturbance predicted by small-amplitude wave theory (§2.2). We then describe the basic experimental details (§3) and observations (§4) that permit quantification of the component terms (§§5–7). In §8, we consider the sum of these component terms at the seafloor and how the sum compares to an alternative estimate derived from the horizontal momentum equation. The distinctive net bottom pressure signature of a train of elevation waves is summarized in §9 and compared to the inferred signature of a train of depression waves. Conclusions (§10) follow.

## 2. Theoretical preliminaries

### 2.1. Definition of the pressure field

In this section, we define the pressure field associated with a two-dimensional wave travelling in the  $x$ -direction with phase speed  $c$ . The vertical component of the momentum equations for a non-rotating inviscid Boussinesq fluid may be written as

$$\frac{\partial p}{\partial z} = -\rho g - \rho_0 \frac{Dw}{Dt}, \quad (2.1)$$

where

$$\frac{D}{Dt} \equiv \frac{\partial}{\partial t} + u \frac{\partial}{\partial x} + w \frac{\partial}{\partial z}. \quad (2.2)$$

For a wave travelling without change of form at phase speed  $c$ , the partial time derivative may be written as

$$\frac{\partial}{\partial t} = -c \frac{\partial}{\partial x}. \quad (2.3)$$

In accordance with the Boussinesq approximation, the pressure anomaly  $p$  and the density anomaly  $\rho$  represent small departures from a reference state in which the density  $\rho_0$  is uniform and pressure is hydrostatic. For now, we neglect viscous terms. In §8, we consider their role at and near the seafloor.

We consider the pressure anomaly to be comprised of a hydrostatic and a non-hydrostatic component, whose vertical gradients are given by the first and second terms, respectively, on the right-hand side of (2.1). To complete the definitions of these pressure components we must consider the boundary conditions at the surface. The vertical coordinate is defined so that  $z=0$  coincides with the seafloor. The undisturbed water depth is given by  $H$ , and the surface displacement is  $\eta_H(x, t)$ , so

that the boundary condition  $p = 0$  (approximating atmospheric pressure) applies at the water surface,  $z = H + \eta_H$ . Assuming that the surface displacement is small enough to justify a first-order Taylor series expansion in depth, we may write the pressure at  $z = H$  as

$$p|_{z=H} = -\eta_H \left. \frac{\partial p}{\partial z} \right|_{z=H+\eta_H} = \rho_0 \eta_H \left( g + \frac{Dw}{Dt} \right) \Big|_{z=H+\eta_H}, \quad (2.4)$$

which becomes

$$p|_{z=H} = \rho_0 g \eta_H \quad (2.5)$$

with the assumption that accelerations of the ocean surface are small in comparison with gravity. This pressure will be referred to as the external hydrostatic pressure due to the wave.

Alternatively, the pressure may be evaluated from the horizontal momentum equation written as

$$\frac{\partial p}{\partial x} = -\rho_0 \frac{Du}{Dt}. \quad (2.6)$$

In particular, the surface displacement is obtained by integrating the horizontal momentum equation along  $z = H$ . Assuming the surface displacement vanishes at  $x = \pm \infty$ ,

$$\eta_H = -\frac{1}{g} \int_{-\infty}^x \frac{Du_H}{Dt} dx', \quad (2.7)$$

where  $u_H$  is the velocity in the direction of wave propagation at  $z = H$ .

We apply separate boundary conditions  $p_h = 0$  and  $p_{nh} = 0$  at the undisturbed surface  $z = H$  (Pedlosky 2003, for example), resulting in

$$p_h = \int_z^H \rho g dz', \quad (2.8)$$

and

$$p_{nh} = \rho_0 \int_z^H \frac{Dw}{Dt} dz'. \quad (2.9)$$

The pressure field defined by (2.8) is termed the internal hydrostatic pressure. Equation (2.9) defines the non-hydrostatic pressure.

Finally, in order to distinguish the wave disturbance from ambient conditions, we define a density profile  $\rho_0 + \rho_U(z)$ † and a wave-driven perturbation  $\rho_W(x, z, t)$ , so that the total density field is  $\rho_0 + \rho_U + \rho_W$ . The internal hydrostatic pressure is partitioned into an ambient profile,

$$p_U = \int_z^H (\rho_0 + \rho_U) g dz', \quad (2.10)$$

and a wave-driven disturbance,

$$p_{Wh} = \int_z^H \rho_W g dz'. \quad (2.11)$$

In summary, the pressure consists of four component fields:

$$p = p_U + p_{Wh} + \rho_0 g \eta_H + p_{nh}, \quad (2.12)$$

† This is the upstream profile in the wave's reference frame. Here after we refer to  $\rho_0 + \rho_U(z)$  as the ambient profile.

which are computed using (2.10), (2.11), (2.7) and (2.9), respectively. Our interest here is in quantifying the perturbation pressure field effected by observed geophysical waves, the sum of the latter three terms on the right-hand-side of (2.12). Pressure signals at the seafloor are of particular interest.

## 2.2. Predictions from small-amplitude wave theory

Before describing the observational results, we look briefly at some salient properties of hydrostatic and non-hydrostatic pressure fields based on a simple theoretical model of weakly nonlinear internal waves. In the limit of small amplitude and long wavelength, internal waves are described by Korteweg–deVries (KdV) theory (Lee & Beardsley 1974; Maslowe & Redekopp 1980; Gear & Grimshaw 1983). While the relevance of this limit for oceanic internal waves is open to question, we will see that the theory provides a useful qualitative picture of the waves' pressure structure.

We assume a two-dimensional flow that is stationary in a reference frame moving with velocity  $c$ . At lowest order, the isopycnal displacement  $\eta$  has the separable form

$$\eta(x, z, t) = A(s)\phi(z), \quad (2.13)$$

where  $s = x - c_0t$  and  $c_0$  is the first-order approximation to the phase velocity. The vertical displacement structure function  $\phi(z)$  is a solution of

$$\frac{d}{dz} \left[ (U - c_0)^2 \frac{d\phi}{dz} \right] + N^2\phi = 0, \quad \phi(0) = \phi(H) = 0. \quad (2.14)$$

The buoyancy frequency  $N(z)$  is derived from the ambient density profile:  $N^2(z) = -g\rho_0^{-1}d\rho_U/dz$  and  $U(z)$  is the ambient velocity profile. The eigenfunction is normalized so that  $\phi(z_0) = 1$ , where  $z_0$  is the level where  $|\phi(z)|$  is a maximum. The velocity components are given by:

$$u = U - \frac{\partial}{\partial z} [(U - c_0)\eta]; \quad w = (U - c) \frac{\partial \eta}{\partial x}. \quad (2.15)$$

The waves of interest here are roughly described by the canonical first baroclinic mode structure, for which  $\phi$  is positive everywhere except at the boundaries and exhibits a single maximum at  $z = z_0$ . Results are easily generalized to higher-order modes.

The function  $A$  is a solution of the KdV equation,

$$(c_0 - c_1)A_s + \alpha AA_s + \beta A_{sss} = 0, \quad (2.16)$$

in which

$$\alpha = -\frac{3}{2} \frac{\int_0^H (U - c_0)^2 (d\phi/dz)^3 dz}{\int_0^H (U - c_0) (d\phi/dz)^2 dz}; \quad \beta = -\frac{1}{2} \frac{\int_0^H (U - c_0)^2 \phi^2 dz}{\int_0^H (U - c_0) (d\phi/dz)^2 dz} \quad (2.17)$$

and  $c_1$  is the second-order phase speed (Gear & Grimshaw 1983). Note that (2.17) incorporates the Boussinesq approximation. A local maximum where  $A > 0$  is called a wave of elevation; a local minimum where  $A < 0$  is called a wave of depression.

We now derive several results pertaining to the hydrostatic and non-hydrostatic pressure fields described in the previous section. The density disturbance associated with the wave may be written as

$$\rho_w = \rho_U(z - \eta) - \rho_U(z) \approx -\eta d\rho_U/dz, \quad (2.18)$$

so that corresponding hydrostatic pressure disturbance (2.11) becomes

$$p_{wh}(s, z) = \rho_0 \int_z^H \eta N^2 dz' = \rho_0 A \int_z^H N^2 \phi dz'. \quad (2.19)$$

For the first baroclinic mode,  $\phi > 0$ . Assuming stable stratification  $N^2 \geq 0$ , the integral in (2.19) is positive (except at the upper boundary, where it vanishes). Thus, the hydrostatic pressure disturbance has the same sign as  $A$ , i.e. positive for a wave of elevation, negative for a wave of depression. Assuming  $N^2 \geq 0$ , the depth of maximum  $p_{wh}$  coincides with  $\phi = 0$ ; thus, for a first baroclinic mode,  $p_{wh}$  is maximized at  $z = 0$ .

The external hydrostatic (surface) pressure is obtained by integrating (2.6) along  $z = H$ , namely,

$$\rho_0 g \eta_H(s) = -\frac{1}{2} \rho_0 (u_H - c_0)^2 \Big|_{-\infty}^s, \quad (2.20)$$

where  $u_H$  is the horizontal velocity at  $z = H$ . Assuming that the surface disturbance vanishes far from the wave, this becomes:

$$\rho_0 g \eta_H(s) = \rho_0 (U_H - c_0)^2 A \phi'_H, \quad (2.21)$$

where  $U_H$  and  $\phi'_H$  are the values of  $U$  and  $d\phi/dz$  at  $z = H$ . For the first baroclinic mode,  $\phi'_H < 0$ , so the sign of the surface pressure is opposite to that of  $A$  (and hence to that of the hydrostatic pressure).

We turn next to the non-hydrostatic pressure disturbance. Equation (2.9), after substitution from (2.15) and (2.13) and neglect of higher-order terms, becomes

$$p_{nh}(s, z) = \rho_0 \frac{d^2 A}{ds^2} \int_z^H (U - c_0)^2 \phi dz'. \quad (2.22)$$

This pressure signal comes entirely from local vertical accelerations; the advective components of  $Dw/Dt$  are negligible. For the first baroclinic mode, the amplitude of the pressure signal is a maximum at the seafloor. Also, since  $\phi > 0$ , the integral in (2.22) is positive (except at the surface, where it vanishes), so that the non-hydrostatic pressure has the sign of the second horizontal derivative of the isopycnal displacement. At the crest (trough) of a wave of elevation (depression),  $d^2 A/ds^2 < 0$  ( $> 0$ ). Like the surface pressure, the peak non-hydrostatic pressure opposes the hydrostatic pressure.

We now specialize further to the well-known soliton solution of the KdV equation:

$$A = a \operatorname{sech}^2 \chi, \quad (2.23)$$

in which  $\chi = (x - c_1 t)/L$  and  $a$  and  $L$  represent the amplitude and length scale, respectively. The constants  $a$ ,  $L$  and  $c_1$  are constrained by two relations:

$$aL^2 = 12 \frac{\beta}{\alpha} \quad c_1 = c_0 + \frac{1}{3} \alpha a. \quad (2.24)$$

For waves of elevation ( $a > 0$ ), the hydrostatic pressure is proportional to  $\operatorname{sech}^2 \chi$ . The same is true of the surface pressure, but with the sign reversed. The non-hydrostatic pressure is proportional to the second derivative:  $-2\operatorname{sech}^2 \chi (1 - 3\tanh^2 \chi)$ . This function is negative at the wave crest. On the flanks of the wave, the second derivative crosses zero and attains symmetric local maxima, revealing a pressure perturbation of opposite sign and 1/3 the magnitude of that found at the wave crest (figure 1).

The total pressure signal is therefore a combination of the  $\operatorname{sech}^2$  form of the hydrostatic and surface components and the more complex form of the non-hydrostatic

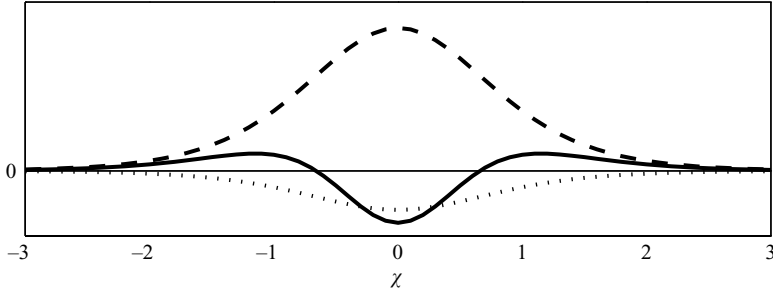


FIGURE 1. Horizontal structure functions for the non-hydrostatic (solid), hydrostatic (dashed) and surface (dotted) pressures due to a solitary wave of elevation. Relative amplitudes are arbitrary, but typical of observations reported in this paper.

component. The relative magnitudes of these contributions to the pressure signal are of considerable importance in the interpretation of oceanographic measurements. Of particular interest is the pressure signal at the seafloor, as sensors can be placed there easily and provide significant information about the internal wave field.

We focus here on the ratio of non-hydrostatic pressure to the sum of hydrostatic and surface pressure signals at the seafloor:

$$R = \left| \frac{p_{nh}(0, 0)}{p_{wh}(0, 0) + \rho_0 g \eta_H(0)} \right| = \frac{a}{a_0}, \quad (2.25)$$

in which

$$a_0 = \left| \frac{\int_0^H N^2 \phi \, dz' + (U_H - c_0)^2 \phi'_H}{2 \int_0^H (U - c_0)^2 \phi \, dz'} aL^2 \right|, \quad (2.26)$$

where the constant  $aL^2$  is given by (2.24) and (2.17). Note that  $c_1$  has been replaced by  $c_0$  in keeping with the small-amplitude long-wavelength approximation.

In summary, small-amplitude theory predicts the following.

(i) The internal and external hydrostatic pressure disturbances have the same horizontal structure as does the isopycnal displacement, i.e.  $\text{sech}^2 \chi$  for a standard soliton.

(ii) For a wave of elevation, the peak internal hydrostatic pressure is positive; the peak non-hydrostatic and external hydrostatic pressures are negative. For a wave of depression, these signs are reversed. The external hydrostatic pressure is independent of depth. For first baroclinic mode waves, the peak non-hydrostatic and internal hydrostatic pressures occur at  $z = 0$ .

(iii) The non-hydrostatic disturbance is driven mainly by local vertical accelerations; advection terms are small.

(iv) The non-hydrostatic disturbance at the sea floor is proportional to the second horizontal derivative of the isopycnal displacement as shown in figure 1.

(v) The ratio of non-hydrostatic to hydrostatic bottom pressures beneath the crest is proportional to the wave's amplitude.

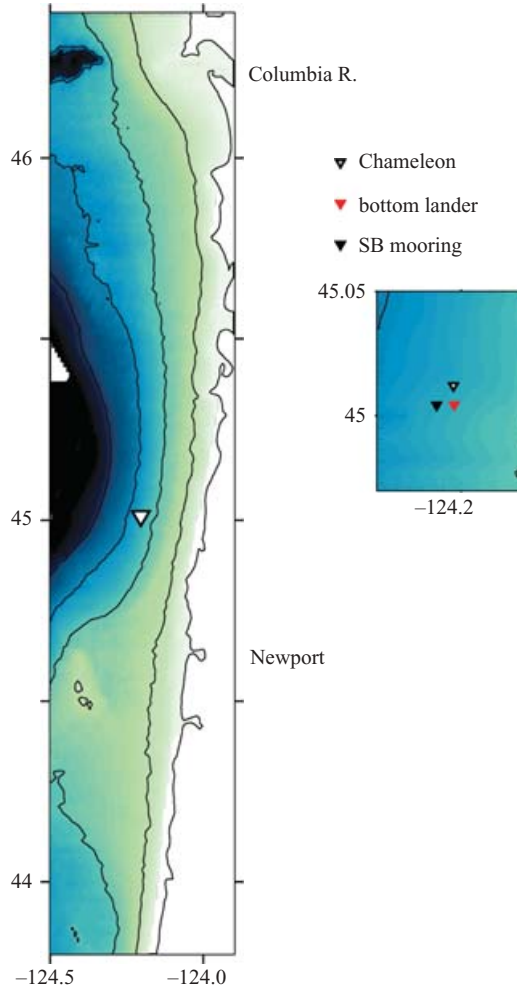


FIGURE 2. Location of the experiment off the Oregon coast in January 2003 (white diamond). Depths are contoured at 50, 100 and 150 m. The inset shows relative locations of CHAMELEON density profile, bottom lander and SB mooring. The lander is 653 m due east of the mooring and 850 m due south of the CHAMELEON density profile. The mean water depth at lander and profiling station is 124 m – the depth at the location of the SB mooring is 5 m greater.

### 3. Experimental details

We discuss observations made in January/February 2003 over the continental shelf off Oregon (figure 2). Most significant for the analysis here is a time series of velocity profiles from an upward-looking 300 kHz acoustic Doppler current profiler (ADCP) mounted on a bottom lander deployed in 124 m water depth. The ADCP rested 1.2 m above the bottom on a gimballed base to ensure vertical orientation. Data were sampled at 1 m vertical intervals; 5 s ensemble averages were recorded. The lander was deployed on 20 January 2003 and data were returned until 22 January. Unfortunately, a storage disk error precluded data recovery past 22 January.

Important ancillary data include extensive density profiling observations made, as part of the same experiment, with our vertical turbulence profiler, CHAMELEON (Moum

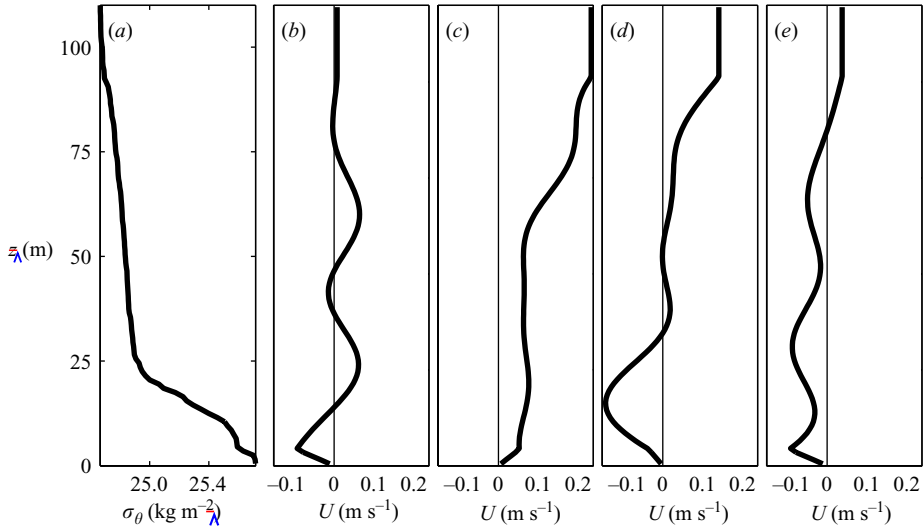


FIGURE 3. Density and velocity profiles assumed to represent ambient conditions. (a) Relative potential density profile  $\sigma_\theta = \rho_\theta - 1000 \text{ kg m}^{-3}$  measured using CHAMELEON at 0145 on 21 January 2003 at the position shown in the inset to figure 2. This profile is nearest in time at this location to the velocity profile time series obtained at the bottom lander site. (b–e) ADCP velocity profiles measured immediately prior to the arrival of each of the four bores shown in figure 4.

*et al.* 1995). A protective ring on CHAMELEON’s nose permitted measurements to the seafloor; density measurements were continuous above 2 cm height. Temperature measurements were made at 1 m above the bottom at the locations of our bottom lander (sampled at 1 s intervals) and a mooring (SB mooring; sampled at 2 min intervals) deployed 653 m offshore of the lander. The positions of each of these measurements is shown in the inset to figure 2.

CHAMELEON observations were made in a nearly continuous set of transects across the shelf at the latitude shown in figure 2 over the period 21 January–05 February 2003. Also, a profiling times series was executed at the position shown by the CHAMELEON triangle from 30 January to 01 February 2003.

#### 4. Observations

Wintertime conditions off Oregon typically consist of northerly winds resulting in a classical downwelling circulation with a broad southward flow ( $0.2\text{--}0.4 \text{ m s}^{-1}$  peak speeds). Superimposed on the mean current structure is a strongly baroclinic tidal ( $M_2$ ) velocity component with peak currents that can reach  $0.1 \text{ m s}^{-1}$ , predominantly across the shelf. A consequence of the downwelling circulation is a relatively deep and well-mixed surface layer and a highly stratified near-bottom interface atop a bottom boundary layer. The density profile shown in figure 3(a) is representative of the vertical structure.

A 22 h record of eastward velocity (figure 4) shows a sequence of 4 wave trains. (The following day, no wave trains were observed.) The range of amplitudes,  $a$ , is 12–33 m. (Wave amplitude was determined as the maximum vertical streamline displacement for each wave. Details of the streamfunction calculation are given in §6.2.) The number of waves in each train is difficult to establish precisely as the signal of the

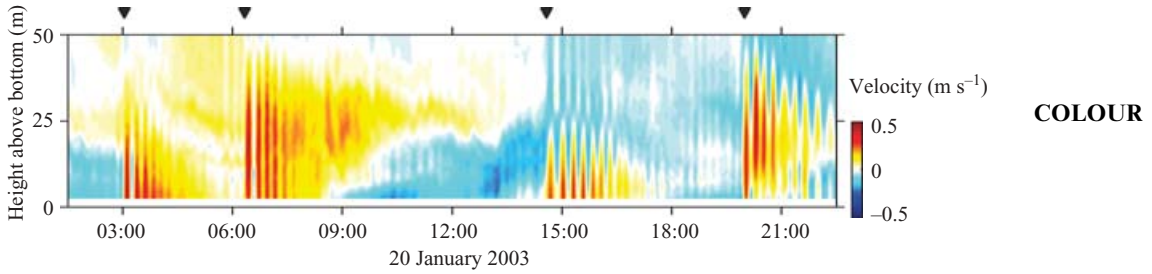


FIGURE 4. Velocity component ( $u$ ) in the direction of wave propagation for a 22 h period on 20 January 2003 showing the passage of four groups of nonlinear internal waves. Inverted triangles indicate the leading edges of the leading waves in each wave train.

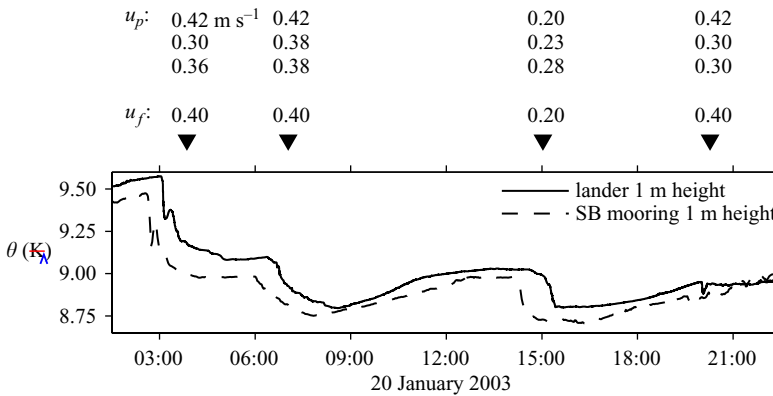


FIGURE 5. Temperature records measured 1 m above the bottom at two locations separated by 653 m on the continental shelf off Oregon. The lander (on which the upward-looking ADCP was deployed from which the velocity measurements shown in figures 6 and 4 were obtained) was due east of the SB mooring where the bottom depth was 5 m shallower. Inverted triangles indicate the leading edges of the leading waves in each wave train shown in figure 4 as determined from velocity measurements.  $u_f$  represents the average speed of the temperature fronts as they passed between the two locations, determined from feature-tracking. The speeds  $u_p$  are the mean fluid speeds measured in the three leading waves from each wave train.

trailing waves diminishes continuously, but the number appears to range between 5 and 11. The final wave train is peculiar in that the waves following the leading wave have no, or greatly diminished, bottom signature.

The wave trains exist within the structure of larger-scale fronts that advect across the shelf. The temperature record from the SB mooring is compared to the lander temperature (both 1 m above the bottom) in figure 5. The times of the wave trains defined from the velocity measurements (noted as inverted triangles above figure 5) coincide (though not exactly) with the passage of the temperature fronts at the lander. These fronts appear associated with an internal bore or gravity current (Moum *et al.* 2005), the wave trains forming at the head. The front speed  $u_f$  is calculated as the average speed of the temperature fronts as they passed between the two locations, determined from feature-tracking.

The velocity structure through the three leading waves of the second wave train in figure 4 are shown in figure 6. The general structure is similar to that described by Moum *et al.* (2003) for a near-surface wave of depression, but inverted. The leading and convergent edge of the wave at the bottom underlies an upward vertical velocity

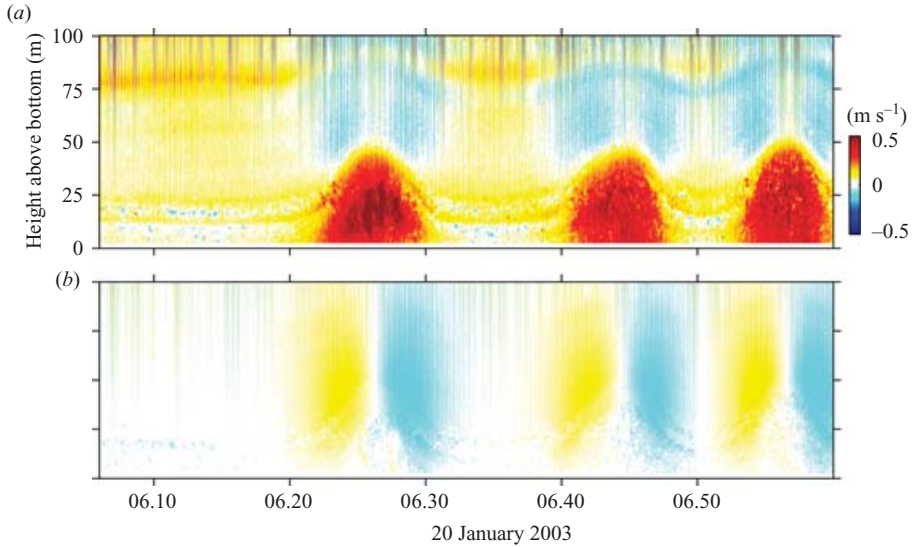


FIGURE 6. Two components of the velocity field measured from an upward-looking ADCP on the sea floor as a sequence of nonlinear internal waves propagates past the site. (a)  $u$ , velocity in the direction of wave propagation (in this case, due east); (b)  $w$ , vertical velocity. The same colour scale is applied to both velocity image plots.

ahead of the wave's velocity core. Above the velocity core, continuity requires a flow in the opposite direction, so that the surface signature of the leading edge of the wave is divergent flow. By comparison, the surface signature of the leading edge of a near-surface wave of depression is marked by convergent flow. This distinction is important for both surface and bottom signatures of each form of wave. Superimposed on the wave's velocity in figure 6 is the 10–12 s swell, which appears as vertical striations. In figure 4 and in all subsequent analyses, this signal is removed by filtering (at 30 s; 8-pole lowpass Butterworth).

#### 4.1. Phase speed

Our calculations of the pressure terms require an estimate of the phase speed for each wave. We were unable to track individual waves and so cannot determine phase speeds directly. Two estimates are discussed here.

Our first estimate was based on the horizontal parcel velocity within the wave crest, whose mean value is denoted as  $u_p$ . Unless the wave is in a state of catastrophic breakdown,  $u_p$  cannot exceed the phase speed. For large-amplitude internal waves, however,  $u_p$  is typically of the same order as  $c$  (e.g. Lamb 2003). Therefore, we regard  $u_p$  as a lower bound on the phase speed. The mean horizontal parcel velocity was determined for the velocity cores within the three leading waves in each wave train depicted in figure 4, 12 waves in all. The velocity cores were defined by the height range [5 m,  $0.6a$ ] and the time range [20 s after the maximum  $du/dx|_{z=0}$  at the wave's leading edge, 20 s before the minimum  $du/dx|_{z=0}$  at the wave's trailing edge]. We note that these parcel velocities are roughly consistent with the advective speeds of thermal fronts ( $u_f$ ) upon which these waves were observed (figure 5).

Our second estimate (and the one we ultimately chose for use in subsequent analyses) is the phase speed  $c_1$  of the first baroclinic mode in weakly nonlinear theory (2.24). This calculation requires estimates of the ambient density and velocity profiles ( $\rho_U(z)$ ,  $U(z)$ ) and of the wave amplitude  $a$ . Lacking individual ambient density profiles,

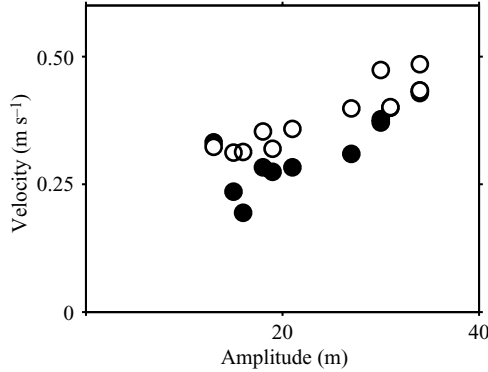


FIGURE 7. ○,  $c_1$  and ●,  $u_p$  versus  $a$  determined for 12 individual waves.

we employed the profile shown in figure 3(a) for all waves (comparison of this density profile to the sequence of density profiles obtained on 30 January indicates relatively weak variation). We assumed that the relevant ambient velocity profile for each wave group was the cross-shelf flow measured just before its arrival at the observation site; hence, we used a separate velocity profile for each of the four wave groups (figure 3b–e). Because the streamfunction calculation (described in §6.2) requires the phase speed as input, the calculation had to be iterated. The parcel speed  $u_p$  was used as a starting value. The iteration converged to within a small fraction of a percent after  $\sim 5$  repetitions, thus furnishing mutually consistent estimates of amplitude and phase speed for each wave.

Figure 7 shows both  $u_p$  and  $c_1$  as functions of  $a$ . As expected, phase speeds exceed parcel speeds. Since this also means that  $c_1 > u_f$ , at the point of observation the waves are propagating more rapidly than the thermal fronts. Hereinafter, we simply refer to  $c_1$  as  $c$ .

## 5. Non-hydrostatic pressure

The high-fidelity velocity measurements obtained by fixing the measurement on the sea floor permit differentiation of the velocity signal to determine the vertical fluid accelerations that contribute to  $p_{nh}$  (equation (2.9)). The computations of  $\partial w/\partial t$  and  $w\partial w/\partial z$  are simply performed by differencing the filtered velocity data, as in figure 8. To evaluate the remaining term, we assume the wave propagates past our measurement point at speed  $c$  without change of form, from which it follows that

$$u \frac{\partial w}{\partial x} = -\frac{u}{c} \frac{\partial w}{\partial t}. \quad (5.1)$$

Using this, we construct the time series

$$\frac{Dw}{Dt} = \frac{\partial w}{\partial t} + u \frac{\partial w}{\partial x} + w \frac{\partial w}{\partial z}. \quad (5.2)$$

The component terms of the vertical fluid acceleration are shown in figure 8 for our example of the leading three waves in figure 6. While details of the structure vary, as do amplitudes, the general structure of each component of vertical acceleration is common to all of the three example waves in figure 8. The local acceleration  $\partial w/\partial t$  is relatively uniform with depth. It changes from positive ahead of the wave core where fluid is accelerated upward to negative above the wave core to positive behind

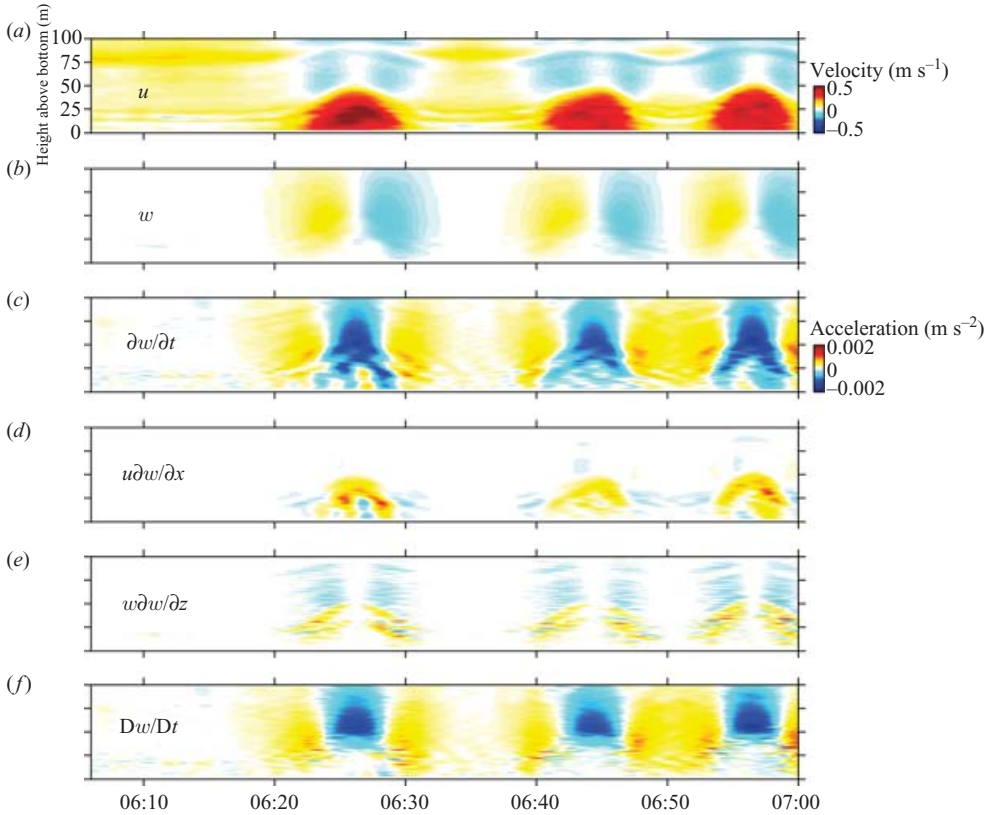


FIGURE 8. (a)  $u$ , (b)  $w$ , as in figure 6, with the signature of the surface swell removed by filtering. The lower three panels show components of vertical fluid acceleration computed from the vertical velocity record: (c)  $\partial w/\partial t$ , (d)  $u\partial w/\partial x$ , (e)  $w\partial w/\partial z$ ; and the total vertical acceleration (f)  $Dw/Dt$ . The same colour scales were applied to each set of velocity and acceleration images.

the wave core (cf. figure 1). As predicted by small-amplitude wave theory (§2.2), this term dominates the vertical integral; its structure thus defines the form of the non-hydrostatic pressure signal at the sea floor (cf. figures 8c and 8f). The advective accelerations are mostly positive and concentrated at the periphery of the wave core.

The non-hydrostatic pressure is computed using equation (2.9). Because of the limitations of the ADCP measurements, data are not available within 24 m of the surface. For these bottom-trapped waves, however, both density and velocity perturbations are greatly attenuated toward the surface, and we assume that both internal hydrostatic and non-hydrostatic pressures vanish above 24 m depth with negligible error. The resulting pressure disturbance is shown in figure 9(a). The amplitude is negative at the wave crest, positive in symmetric regions about the crest, and has maximum amplitude at the seafloor.

The non-hydrostatic pressure at the seafloor is  $p_{nh}^o(x) = p_{nh}(x, z=0)$ .<sup>†</sup> The bottom pressure signature is shown in figure 9(b). Leading and trailing positive pressure

<sup>†</sup> Although our measurements are time series, we have found it instructive to represent local (that is, for a single wave) computations of wave pressure as spatial series. To do this, we set  $x = -c(t - t_0)$ , where  $t_0$  is the time when the wave crest passed the observation site.

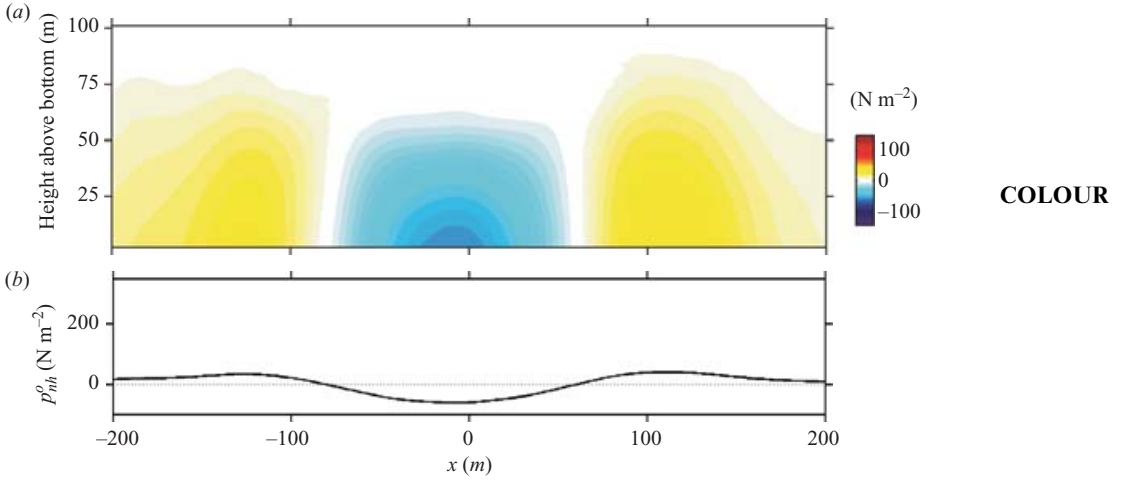


FIGURE 9. (a)  $p_{nh}(x, z)$  computed for the leading wave of figure 8. (b)  $p_{nh}^o(x)$ .

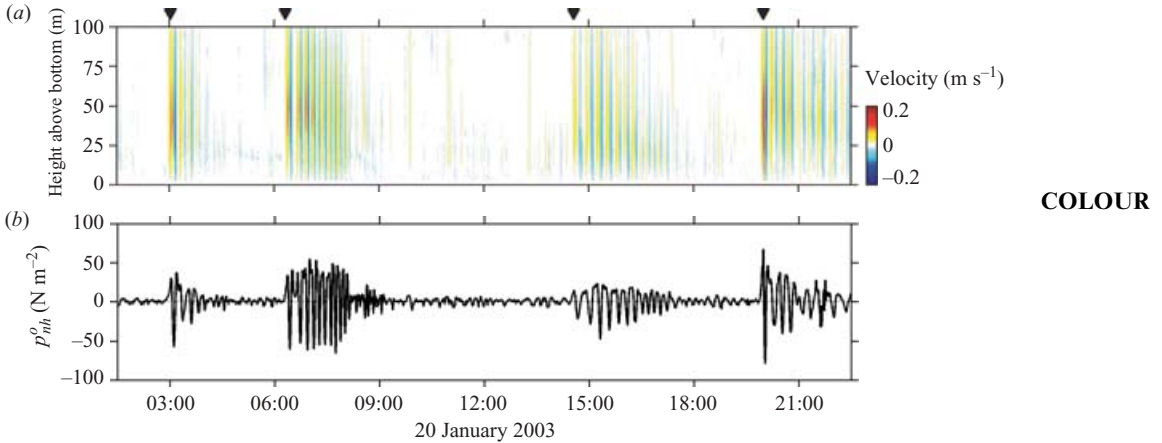


FIGURE 10. (a) Vertical velocity showing the passage of the four wave trains (marked by the inverted triangles above). (b)  $p_{nh}^o(t)$ .

perturbations bound a negative pressure perturbation beneath the wave core. This signature is clearly repeated over the 22 h period (figure 10), though with varying amplitude and duration. The structure of  $p_{nh}^o$  through a single wave is as expected on the basis of small-amplitude theory (figure 9b; cf. figure 1). The ratio of positive to negative peak amplitudes is somewhat greater than the value  $1/3$  predicted in §2.2.

## 6. Internal Hydrostatic Pressure

Unfortunately, we do not have simultaneous velocity and density measurements to determine both  $p_{nh}$  and  $p_{wh}$  directly. We do have density measurements that permit non-simultaneous direct estimates of  $p_{wh}$ . These estimates provide a guide to the expected internal hydrostatic pressure perturbation. We then make an indirect assessment of  $p_{wh}$  by mapping streamlines to isopycnals so that  $p_{wh}$  and  $p_{nh}$  are estimated simultaneously.

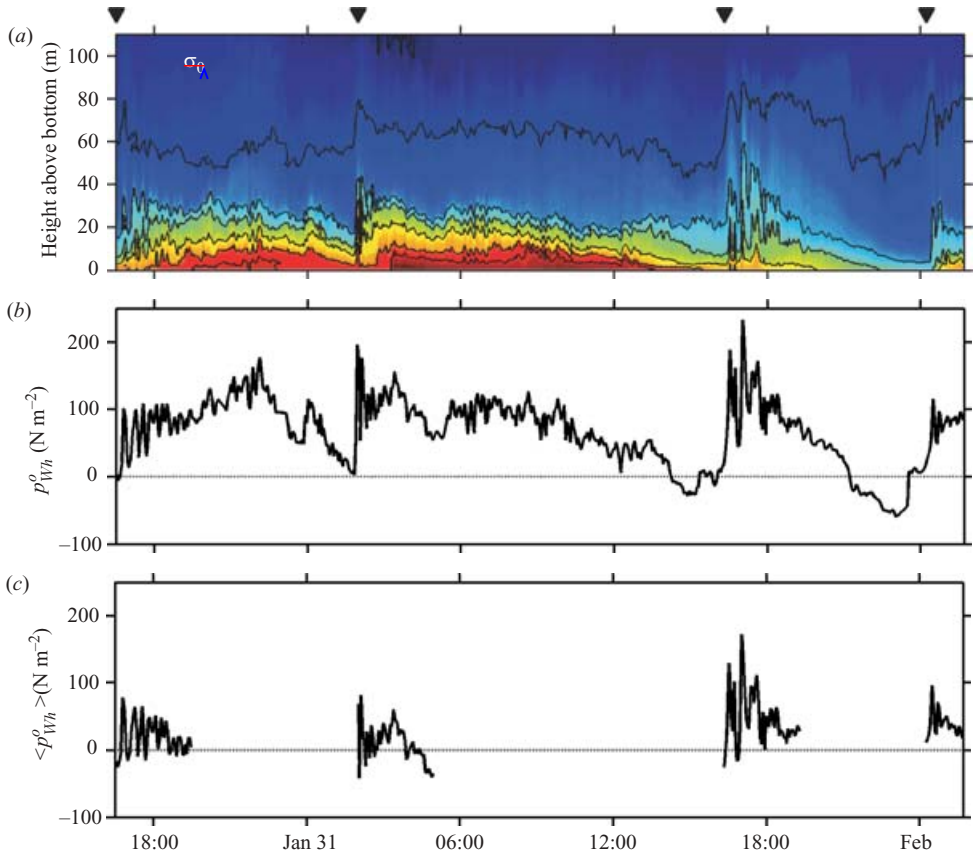


FIGURE 11. (a) Time series of  $\sigma_\theta$  (contours at  $0.2 \text{ kg m}^{-3}$  intervals). (b) Local seafloor hydrostatic pressure, determined relative to a reference time period immediately preceding each bore. (c) Hydrostatic pressure perturbations, determined by filtering to emphasize fluctuations due to the waves only.

### 6.1. Determination of $p_{Wh}$ from density profiles

Trains of nonlinear internal waves of elevation were a ubiquitous part of the near-bottom flow field during January 2003, and the density structure of the waves shown in figure 11(a) on 31 January (as well as their high-frequency acoustic backscatter structure; Moum *et al.* 2005) is similar to what we might expect from the velocity data on 20 January. Amplitudes, number of waves in a group, and wavelengths were all similar, as was the ambient density profile (figure 3). We use these examples to determine  $p_{Wh}$  directly.

The perturbation density profile  $\rho_w(z)$  is defined as the deviation from an ambient density profile  $\rho_U$ , defined as the average of four profiles measured immediately prior to the arrival of the wave. The internal hydrostatic pressure perturbation is then given by (2.11); its value at the sea floor is  $p_{Wh}^o(x) = p_{Wh}(x, z=0)$ . Density variations due to the larger scale shelf circulation also cause  $p_{Wh}^o$  to vary. This is seen in figure 11(b), in which  $p_{Wh}^o$  is reset ahead of each wave train where each new ambient density profile is defined. We are concerned here only with the pressure perturbations due to the waves at the leading edge of each density front (noted by the inverted triangles above figure 11a) and assess their value by highpass filtering the signal in figure 11(c)

COLOUR

Q1

at 3 h (4- pole Butterworth). The filtered signal is denoted  $\langle p_{wh}^o \rangle$  (figure 11c), which represents wave-induced internal hydrostatic pressure perturbations; these range from about 50 to 150 N m<sup>-2</sup>

### 6.2. Determination of $p_{wh}$ from streamlines

To estimate internal hydrostatic pressure perturbations in waves for which we have velocity but no corresponding density measurements, requires two significant assumptions. First, the density profile shown in figure 3 is assumed to be representative of ambient conditions found ahead of the waves. Secondly, we assume that the waves are inviscid, two-dimensional and propagate without change of shape with a known speed and direction. In this case, mass conservation implies that streamlines calculated in the wave's reference frame are parallel to isopycnals. The density field may therefore be calculated by extending the ambient density values along streamlines.

The simplest estimate of the streamfunction is obtained by vertical integration of the horizontal velocity:

$$\psi_u(x, z) = \int_0^z (u(x, z') - c) dz'. \quad (6.1)$$

We may also calculate the streamfunction as

$$\psi_{wL}(x, z) = \psi_u(x_L, z) - \int_{x_L}^x w(x', z) dx', \quad (6.2)$$

or

$$\psi_{wR}(x, z) = \psi_u(x_R, z) + \int_x^{x_R} w(x', z) dx', \quad (6.3)$$

in which  $x_L$  and  $x_R$  are locations upstream and downstream of the wave. In a perfectly two-dimensional flow with no measurement errors, these three estimates would be equal. Here,  $\psi_{wL}$  and  $\psi_{wR}$  are regarded as less reliable because they require the use of  $\psi_u$  as a boundary condition. This uncertainty is reduced by defining a combined estimate:

$$\psi_w = 0.5(\psi_{wL} + \psi_{wR}), \quad (6.4)$$

which is then averaged with  $\psi_u$  to obtain the final estimate:

$$\psi = 0.5(\psi_u + \psi_w). \quad (6.5)$$

Velocity components derived from this streamfunction generally match measured velocities to within 2–3 cm s<sup>-1</sup>.

The perturbation density field was determined by extending density values from the assumed ambient profile along streamlines, then subtracting the ambient profile. The internal hydrostatic pressure perturbation is then given by (2.11).

The resulting internal hydrostatic pressure perturbation determined for the example wave shown in figure 9 is nearly positive definite. It rises to a maximum value at the seafloor beneath the wave crest (figure 12a, b). This maximum value is denoted  $\max_x p_{wh}^o$ . Values of  $\max_x p_{wh}^o$  ranged from 100 to 300 N m<sup>-2</sup>.

To assess the uncertainty in our estimate of  $p_{wh}$  owing to imprecise knowledge of  $c$ , we compare the bottom pressure computed using the phase speed  $c_1$  with that found using the lower bound  $u_p$  (figure 7). Use of  $u_p$  increases our estimate of the hydrostatic pressure by about 15%.

To assess the uncertainty due to imprecise knowledge of the streamfunction, we recompute the profile  $p_{wh}^o(x)$  for the three estimates  $\psi_u$ ,  $\psi_w$  and  $\psi$  (figure 13b). Both

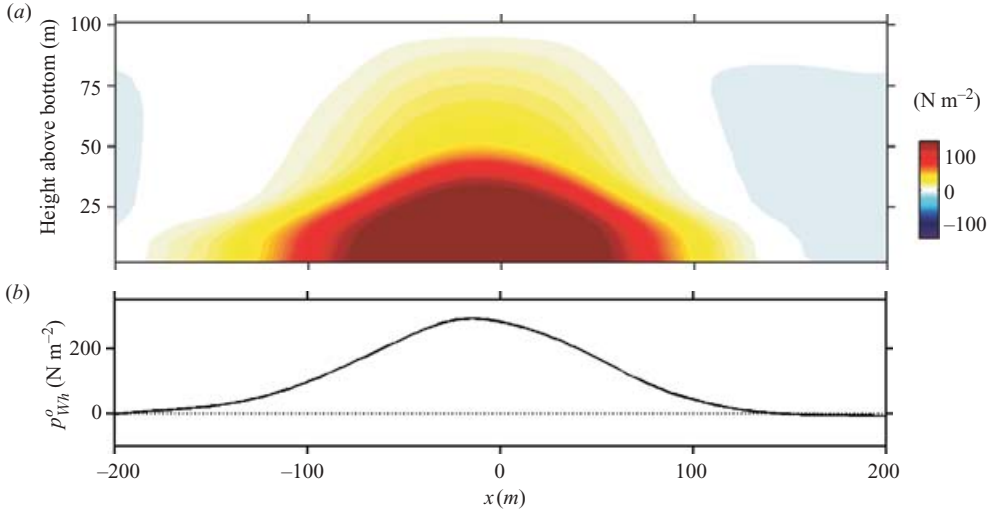


FIGURE 12. (a)  $p_{Wh}(x, z)$  computed for the leading wave of figure 8. (b)  $p_{Wh}^o(x)$ , the wave-driven internal hydrostatic pressure at the sea floor.

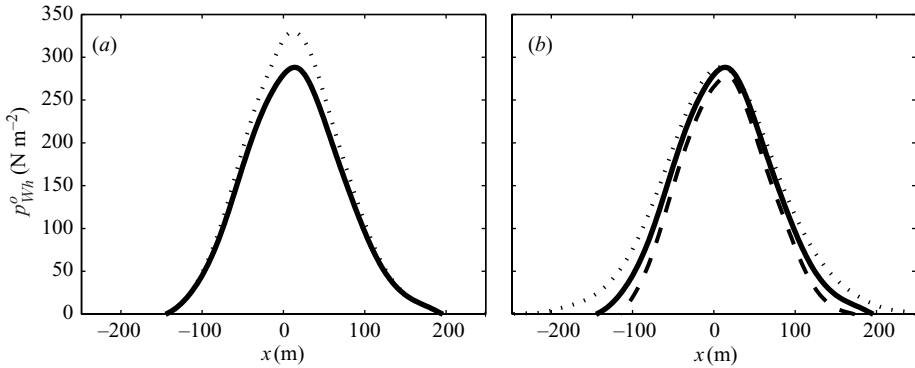


FIGURE 13. Sources of uncertainty in the bottom hydrostatic pressure. (a) Dependence on the estimated phase velocity. Solid curve:  $p_{Wh}^o$ , computed using our best estimate,  $c_1 = 0.49 \text{ m s}^{-1}$ . Dotted curve:  $p_{Wh}^o$  computed using the lower bound  $u_p = 0.43$  for the phase speed. (b) Dependence on the assumed streamfunction. Pressure was computed using  $\psi_u$  (dashed curve),  $\psi_w$  (dotted curve) and  $\psi$  (solid curve).

the amplitude and the width of the seafloor pressure signal are affected by our choice of streamfunction. The effect on amplitude is about 5%.

We conclude that these estimates of the hydrostatic pressure are uncertain by about 20%. For the seafloor values shown in figure 13, the uncertainty is about  $60 \text{ N m}^{-2}$ .

In summary, we have made two estimates of  $p_{Wh}$ , one direct but not coincident with our velocity measurements, the second coincident but indirect. In the first case, peak values of  $p_{Wh}^o$  range from 50 to  $150 \text{ N m}^{-2}$ ; in the second case from 100 to  $300 \text{ N m}^{-2}$ . The direct estimate is based on a sequence of density profiles, each separated by roughly five minutes. The duration of individual waves shown in figure 6 is less than 10 minutes. We have, therefore, undersampled isopycnal variability created by the waves and hence, their internal hydrostatic pressure perturbation – this results in an underestimate of peak values. By comparison, despite other shortcomings discussed

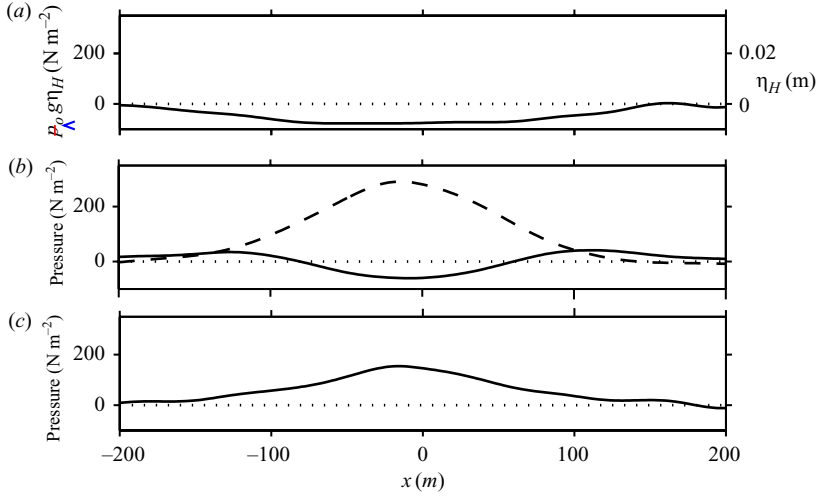


FIGURE 14. (a) Surface displacement (ordinate scaled for both displacement and pressure) computed from the near-surface velocity field for the leading wave shown in figure 6. (b)  $p_{nh}^o$  (solid line),  $p_{wh}^o$  (dashed line). (c) Total pressure perturbation at the sea floor,  $p_{hh}^o + p_{wh}^o + \rho_0 g \eta_H$ .

above, the indirect estimate of  $p_{wh}$  benefits from a continuous record (5 s sampling). Aside from any problems in determination of  $p_{wh}$ , it is quite possible that variations in the amplitudes of the waves between the two sampling periods account for the differences in  $p_{wh}$ .

## 7. Surface displacement

The surface displacement  $\eta_H(x)$  caused by the wave is estimated by integration along  $x$  of the measured horizontal fluid acceleration at the surface (equation (2.7)), using a method similar to that described in § 5. Two limitations arise. First, reliable velocity measurements can only be made to within 24 m of the surface. (Reflection of the side lobes of the acoustic transducer contaminates measurements near acoustically reflecting surfaces, the free surface being an example.) However, we expect the difference in velocity between the surface and 24 m to be relatively small in these bottom-trapped waves and assume that, for our purpose, they are equal. More serious is the matter of ADCP beam-spreading as a function of range. At 100 m range (24 m depth), beam separation is about 70 m, a significant fraction of the wavelength. This means that a velocity measurement will average over the maximum gradient region. This can be minimized by recording along-beam velocities (Scotti *et al.* 2005) and then converting to geographical coordinates (not done here) and by sampling rapidly (which was done here). The result is a wavelength-dependent underestimate of the gradients of horizontal velocities at large ranges, and hence of  $\eta_H(x)$ . Subsampling a  $\text{sech}^2(x)$  model of the surface velocity field suggests the underestimate in the surface convergence to be 20% at 100 m wavelength.

Integration along  $x$  produces a negative displacement at the divergent leading edge, forming a surface depression above the wave crest (figure 14a). Behind the crest, continued integration along the convergent trailing edge reduces the depression to 0. The maximum displacement is approximately 0.007 m (in equivalent pressure units, about  $70 \text{ N m}^{-2}$ ). The range of  $\max_x \eta_H$  from all of the twelve

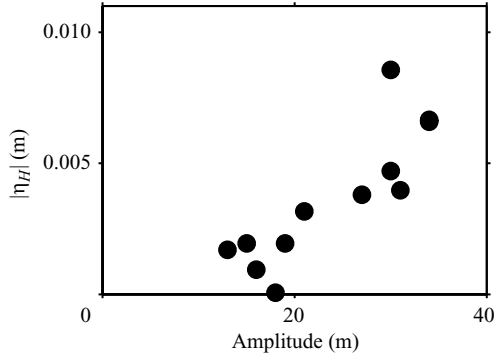


FIGURE 15.  $\eta_H$  vs.  $a$ . The linear correlation coefficient,  $r = 0.85$  [0.54, 0.96], is given with 95% confidence limits.

waves examined is 0.0001–0.009 m and increases monotonically with increasing wave amplitude (figure 15). Again, this must be an underestimate of the maximum surface displacement.

## 8. Wave pressure disturbance at the seafloor

Figure 14(b) shows the internal hydrostatic and non-hydrostatic bottom pressures and figure 14(c) the net bottom pressure evaluated at the seafloor for our example wave. Here, the hydrostatic component dominates and the net pressure perturbation is therefore positive definite. Comparison of figure 14(b) with figure 1 indicates agreement of the observed horizontal structure with that predicted on the basis of small-amplitude theory.

An independent estimate of seafloor pressure is obtained by horizontal integration of (2.6) near the seafloor. Until now, we have ignored the fact that our velocity measurements begin not at  $z=0$ , but 2 m above the bottom, and we have assigned the lower limits of the vertical integrals to  $z=0$ . While  $w$  at  $z=2$  m is greatly diminished from its values higher in the water column and hence the distinction is unimportant,  $u$  can be quite large at  $z=2$  m (up to  $0.4 \text{ m s}^{-1}$ ) whereas it must vanish at  $z=0$ . First, we consider the pressure obtained by integration of (2.6) at  $z=2$  m to represent that at  $z=0$ . We then consider the consequence of  $u(z=0)=0$ .

$$p_{Du/Dt}^o = -\rho_0 \int_{-\infty}^x \frac{Du}{Dt} \Big|_{z=2m} dx' \quad (8.1)$$

is compared to the sum  $p_{Wh}^o + p_{nh}^o + \rho_0 g \eta_H$  in figure 16. These estimates indicate  $p_{Du/Dt}^o \simeq 0.55(p_{Wh}^o + p_{nh}^o + \rho_0 g \eta_H)$ .

One reason for the difference in the two estimates of seafloor pressure perturbation is our certain underestimate of  $|\eta_H|$  owing to ADCP beam spreading. Since  $\eta_H < 0$ , this produces a high bias to our estimate of positive seafloor pressure from a vertical momentum balance. An underestimate of  $\rho_0 g \eta_H$  by a factor of 2 would approximately satisfy the inequality shown in figure 16; however, it is unlikely that the error is this large (recall that we estimate it to be 20%).

Perhaps an alternative explanation for the difference in the two estimates of seafloor pressure perturbation is associated with an additional term not considered in (8.1). We first consider the limiting case, at the seafloor, and then the consequence of an imbalance immediately above the seafloor. At the seafloor  $z=0$ ,  $u=0$ , and we cannot

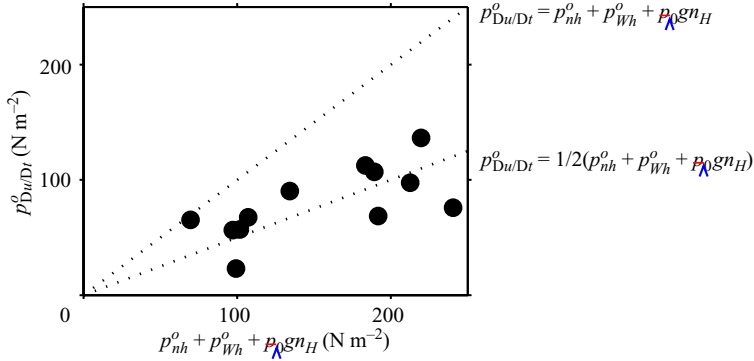


FIGURE 16. Comparison of total pressure evaluated at the seafloor by integration of vertical (abscissa) and horizontal (ordinate) momentum equations.

consider the fluid to be inviscid; the horizontal momentum equation is

$$\frac{\partial p}{\partial x} = \frac{\partial \tau}{\partial z}, \quad (8.2)$$

$\tau$  representing the turbulent stress, which we consider to be most significant in terms of its vertical divergence. Since the seafloor value of  $\partial p/\partial x$  changes sign across the wave (figure 14), so must  $\partial \tau/\partial z$ . If  $\tau$  is represented by the product of a positive definite eddy viscosity ( $K_v$ ) and the velocity gradient,

$$\tau = K_v \frac{\partial u}{\partial z}, \quad (8.3)$$

there must either be a change in slope of the vertical gradient of  $K_v$  or a change in curvature of the near-bottom velocity profile (if the latter, we cannot detect it from our observations above 2 m height). This is similar to the case of a steady flow in the boundary layer over an obstruction, for which the pressure gradient changes sign at the summit (Kundu 1990, for example).

In considering the seafloor balance of horizontal momentum, we might also suspect that the turbulence stress divergence contributes to the balance at 2 m height, with the potential of improving the correspondence shown in figure 16. Future observations will address this issue.

## 9. Signatures at seafloor and surface

Large-amplitude nonlinear internal waves exhibit distinctive surface and seafloor signatures, determined by the velocity field and the stratification. Some of the characteristics that distinguish elevation waves from depression waves are clear. Some are less so. It is considerably more difficult to obtain such a clear measurement of near-surface velocities induced by surface-trapped depression waves as we have obtained for these bottom-trapped elevation waves, because of the relative difficulty of making high-fidelity measurements from either a surface vessel or mooring, both of which are contaminated by motions of the free surface. Here, we infer surface and seafloor signatures of surface-trapped depression waves by analogy.

### 9.1. Surface signature

The alternate convergent/divergent surface flow induced by a nonlinear internal wave produces two related but distinct surface expressions. The first is the surface

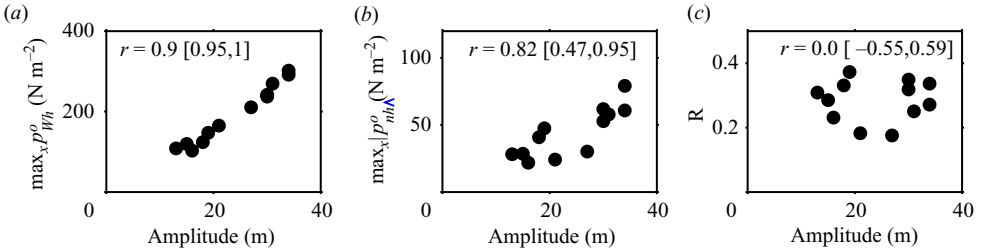


FIGURE 17. (a)  $\max_x p_{Wh}^o$  vs.  $a$ . (b)  $\max_x |p_{nh}^o|$  vs.  $a$ . (c)  $R$  vs.  $a$ .

displacement, related to the flow convergence at the surface via (2.7). For the waves of elevation examined here, we have estimated this to range up to a value of order 0.01 m. The more noticeable surface expression is the modulation of the gravity/capillary wave field, enhanced in convergent flow and diminished (to the extent of producing a nearly flat surface) in divergent flow. This results in a visible twinkling at the convergent edge of a depression wave (Moum *et al.* 2003), and a clear radar signature both from a surface vessel and from space (Fu & Holt 1982). Indeed, detection of nonlinear internal waves from spaceborne SAR has shown their ubiquity and has provided considerable guidance toward determining generation mechanisms (<http://www.internalwaveatlas.com/>). The surface expression of bottom-trapped internal waves will diminish as the water column becomes deeper. However, at least in 124 m of water, it does exist. In the present examples, the surface divergence/convergence is of order  $5 \times 10^{-4} \text{ s}^{-1}$ . While this is an order of magnitude smaller than that found for the surface-trapped waves of Moum *et al.* (2003), its signature may yet be observable.

### 9.2. Seafloor signature

The structure of the components of the perturbation pressure field at the sea floor through our example wave is summarized in figure 14(a, b). Summed, the non-hydrostatic bottom pressure perturbation,  $p_{nh}^o$ , plus the internal hydrostatic pressure perturbation,  $p_{Wh}^o$ , and external hydrostatic pressure perturbation,  $\rho_0 g \eta_H$ , comprise the total bottom wave perturbation pressure signal (figure 14c). For this example, the result is a positive pressure perturbation at the sea floor.

A comparison of peak values of  $p_{Wh}^o$  and  $p_{nh}^o$  indicates a tendency for each to increase with  $a$  (figure 17a, b). The tendency of the ratio  $R$  is not clear, but it is certainly  $< 1$  (figure 17c) (as defined here,  $R$  is an underestimate, since we have underestimated  $\eta_H$ ). We note that a value of  $R = 1$  means that the non-hydrostatic wave pressure exactly balances the total hydrostatic pressure, leaving no seafloor signal. A value  $R > 1$  indicates a strongly non-hydrostatic wave, so that the seafloor pressure perturbation is negative, rather than positive.

We turn next to a comparison of the relative magnitudes of the non-hydrostatic and hydrostatic pressure components with the predictions of small-amplitude theory as described in §2.2. This comparison requires that we compute the amplitude scale  $a_0$  using profiles of ambient density and velocity for each wave. As above, the ambient density profile for all waves was that shown in figure 3(a). We then assumed that each wave group (or bore) propagates in the cross-shelf flow measured just before its arrival at the observation site (figures 3b–d). This assumption results in a different value of  $a_0$  for each wave site group, and thus allows better comparison between the available observations and small-amplitude theory (figure 18).

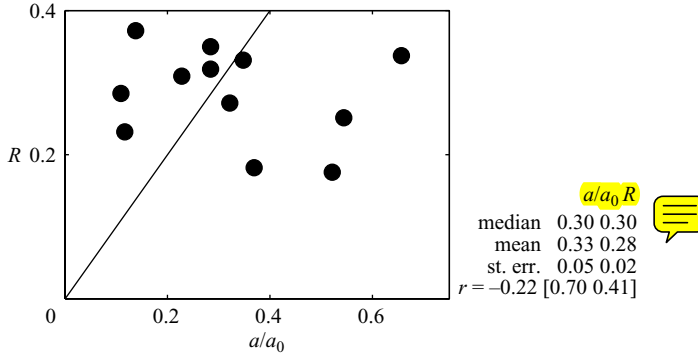


FIGURE 18. Ratio of non-hydrostatic to (external plus internal) hydrostatic bottom pressure versus wave amplitude scaled by  $a_0$ , as described in §2.2. The density profile is that shown in figure 3(a); the ambient velocity is recalculated for each wave group from ADCP measurements (figure 3b–e). Small-amplitude theory predicts  $R = a/a_0$ , as shown by the straight line.

The observed values of  $R$  and the predicted values ( $a/a_0$ ) are both distributed about the median value 0.3. The observed and predicted mean values are similar to this, and agree with each other to within standard error. Deviations about the mean, however, are not well correlated; in fact, their correlation is statistically insignificant. The theoretical values show a standard deviation of 0.17, while the standard deviation for measured values is only 0.07. This could mean that, contrary to the theoretical prediction, there is no relationship between  $R$  and wave amplitude, as figure 17 would seem to suggest. There is, however, too much uncertainty in the present results to justify this conclusion. Measurement errors such as those due to beam spreading cannot account for the degree of scatter in figures 17 and 18, but significant assumptions have been made in interpreting those measurements, both for the purpose of estimating the pressure components and for the purpose of evaluating the predictions of weakly nonlinear theory. To estimate pressure components, we have assumed that the wave is two-dimensional and propagates with a fixed, known phase velocity. We have also assumed that the density profile shown in figure 3a is representative of the entire observation period. To apply weakly nonlinear approximations, we have assumed that the wave propagates in an unchanging environment with known vertical profiles of both density and velocity. In fact, the coastal environment is highly energetic, with wave motions on a range of temporal and spatial scales influencing the propagation of the high-frequency waves discussed here. More comprehensive measurements, and possibly a more realistic theory, will be needed to develop a sound understanding of the component pressures and their dependence on wave amplitude.

### 9.3. Signatures of near-surface waves of depression

Our analysis reveals a distinctive structure of the seafloor pressure record owing to the passage of a train of nonlinear internal waves of elevation (figure 19a). This structure is a direct consequence of the velocity field in the waves, the stratification and the relative magnitudes of  $p_{nh}^o$ ,  $\rho_0 g \eta_H$  and  $p_{Wh}^o$ . The net positive pressure disturbance arises from the dominance of the internal hydrostatic pressure perturbation. By comparison, component pressure perturbations at the seafloor beneath a train of near-surface waves of depression will have a similar structure, but of opposite sign (figure 19b). Under typical conditions, the near-surface velocities of surface-trapped waves are

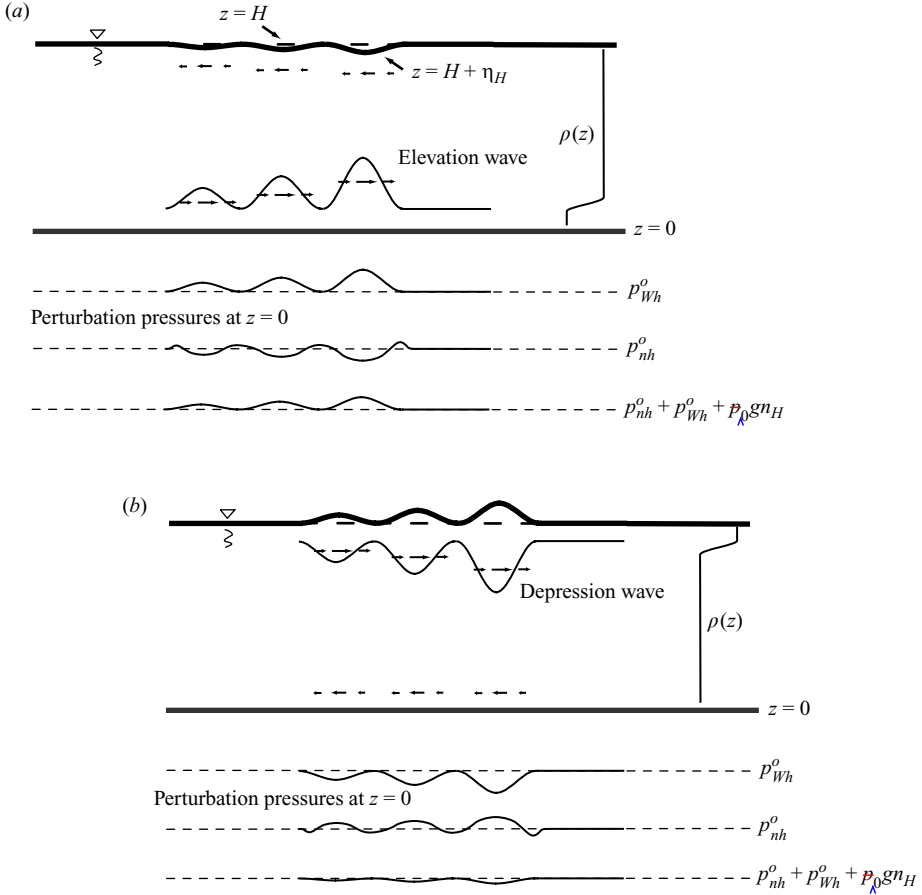


FIGURE 19. (a) Schematic showing surface displacement (exaggerated) and internal (hydrostatic and non-hydrostatic) pressure in a train of three waves of elevation propagating to the right as deduced from our measurements. The arrows represent relative speeds across the wave fronts and induced speeds near the surface. (b) Analogous structure inferred for a train of three depression waves. In the depression wave, the inferred surface displacement is relatively larger and the net seafloor pressure signal relatively smaller.

much greater than those of bottom-trapped waves. This is also true of the surface divergences/convergences (see figure 1 from Moum *et al.* 2003, for example). As a result, the magnitudes of surface displacements must be relatively greater via equation (2.6) (for comparison, Pinkel (2000) estimated 0.2 m positive surface displacements in large-amplitude ( $> 60$  m) deep-water solitary waves of depression propagating across the equator). Consequently, the external hydrostatic pressure, which opposes  $p_{Wh}$ , is relatively larger, with  $R$  tending to 1. This will tend to reduce the net seafloor pressure signature, which is, of course, evident in the reduced relative lateral acceleration there. A competing factor, that near-surface stratification is typically greater than near-bottom stratification, will tend to increase  $p_{Wh}^o$ , thereby increasing the net seafloor pressure signature. In infinitely deep water the seafloor pressure of a depression wave vanishes. In sufficiently deep water the signal will be below detection limits.

Another factor that is not clear is the geophysical range of  $R$ . In the waves we have observed,  $p_{Wh}^o$  clearly dominates the net seafloor wave perturbation pressure and

is 3–5 times greater than  $p_{nh}^o$ . If our estimates of  $R$  are typical of depression waves, their signature will be a negative pressure perturbation at the seafloor.

## 10. Conclusions

Measurements taken over the Oregon continental shelf reveal bottom-trapped waves of elevation. We have inferred  $p_{nh}$  and  $\eta_H$  from measured accelerations, and  $p_{wh}$  by mapping isopycnals to measured streamlines. Spatial structures of the component pressure fields are described well by the small-amplitude theory discussed in §2.2. Peak values of  $p_{nh}^o$  are  $< 0$ ,  $\eta_H < 0$  and  $p_{wh}^o > 0$ . Observations confirm that the non-hydrostatic pressure is mainly associated with local vertical accelerations.  $max_x |p_{nh}^o|$ ,  $max_x |\eta_H|$  and  $max_x p_{wh}^o$  increase monotonically with wave amplitude.

Particular attention was paid to the ratio of peak non-hydrostatic to hydrostatic pressures at the seafloor,  $R$ , whose value determines the form of the net bottom pressure. In the observed range  $R \simeq 0.2$ – $0.4$ , the bottom pressure signature of elevation waves is characterized by a sequence of positive pressure perturbations. By direct analogy (which may not be strictly correct), similar conditions will result in a sequence of negative seafloor bottom pressure perturbations for depression waves in shallow water. While the small-amplitude theory described in §2.2 provides a useful qualitative description of the pressure fields and predicts a median value  $R = 0.3$  that is in good agreement with observations, it is inadequate to predict variations of  $R$  with wave amplitude. Improved theoretical predictions will most likely result from more complete measurements of ambient density and velocity profiles. These results also emphasize the importance of establishing the geophysical range of  $R$  via direct observation.

Peak values of  $p_{nh}^o$  ranged from  $-25$  to  $-90 \text{ N m}^{-2}$ , of  $\rho_0 g \eta_H$  from  $-10$  to  $-90 \text{ N m}^{-2}$  and of  $p_{wh}^o$  from  $100$  to  $300 \text{ N m}^{-2}$ . The sum of these ( $O(100) \text{ N m}^{-2}$ , equivalent to about  $1 \text{ cm}$  of water or  $0.015 \text{ p.s.i.}$ ) is a measurable signal. While these waves were not sensed by the relatively crude pressure sensors on our ADCP, they have sufficiently large seafloor pressure signals that they can be detected with currently-available commercial pressure sensors (which claim resolution better than  $1 \text{ mm}$  of water). It is possible that new types of inexpensive seafloor wave antennae can be deployed to investigate more thoroughly the origin, evolution and climatology of these waves.

Nonlinear internal waves of elevation in relatively deep water exhibit significantly smaller (though non-zero) surface signatures than near-surface depression waves. This probably precludes an equivalent spaceborne mapping of elevation waves in a manner employed for depression waves. As elevation waves shoal, their surface expression presumably strengthens, so that detection in shallow water may be possible (Zhao *et al.* 2004). The distinction between the two forms is clear: while a depression wave twinkles at its leading edge and is therefore more reflective there, an elevation wave twinkles at its trailing edge.

Finally, surface pressure measurements have long been used in atmospheric studies, to detect the presence and surface structure of non-hydrostatic flows (across mountain ranges, for example Bougeault *et al.* 1997). In particular, surface pressure measurements have clearly defined the ‘Morning Glory’ (Smith, Crook & Roff 1982) and related waves (Fulton, Zrnica & Doviak 1990). However, all of the atmospheric studies lack the detailed observations of the internal structure of the flows to discern the component pressure perturbations. With the detailed observations made of bottom-trapped waves discussed herein, we have been able to diagnose these components. With the exception of an external hydrostatic pressure disturbance in

the atmosphere (owing to the lack of an equivalent free surface), we expect the roles of internal hydrostatic and non-hydrostatic pressures to be similar.

This work was funded by the National Science Foundation, and by the Office of Naval Research. The participation of W.D.S. was supported by the National Science Foundation via award OCE-0221057. The technical assistance of Alexander Perlin, Mike Neeley-Brown, Ray Kreth, Jody Klymak and Greig Thompson is gratefully acknowledged. We thank Murray Levine, Tim Boyd and Mike Kosro for the bottom temperature record from the SB mooring. Conversations with Jonathan Nash and Greg Avicola were most helpful. Jody Klymak and Alexander Perlin made useful comments on an early draft.

#### REFERENCES

- APEL, J. R., BADIOY, M., CHIU, C.-S., FINETTE, S., HEADRICK, R., LYNCH, J. F., NEWHALL, A., ORR, M. H., PASEWARK, B. H., TIELBUERGER, D., TUGNUTT, A., VON DER HEYT, K. & WOLF, S. 1995 An overview of the 1995 swarm shallow-water internal wave acoustic scattering experiment. *IEEE J. of Oceanic Engng*, **22**, 465–500.
- APEL, J. R., HOLBROOK, J. R., LIU, A. K. & TSIA, J. J. 1985 The Sulu Sea internal soliton experiment. *J. Phys. Oceanogr.* **15**, 1625–1651.
- BOGUCKI, D., DICKEY, T. & REDEKOPP, L. G. 1997 Sediment resuspension and mixing by resonantly generated internal solitary waves. *J. Phys. Oceanogr.* **27**, 1181–1196.
- BOUGEAULT, P., BENECH, B., BESSEMOULIN, P., CARISSIMO, B., CLAR, A. J., PELON, J., PETITDIDIER, M. & RICHARD, E. 1997 PYREX: A summary of findings. *Bull. Am. Met. Soc.* **78**, 637–650.
- CHRISTIE, D. R., MUIRHEAD, K. J. & CLARKE, R. H. 1981 Solitary waves in the lower atmosphere. *Nature* **293**, 46–49.
- CLARKE, R. H., SMITH, R. K. & REID, D. G. 1981 The Morning Glory of the Gulf of Carpentaria: an atmospheric undular bore. *Mon. Weather Rev.* **109**, 1726–1750.
- FU, L. L. & HOLT, B. 1982 Seasat views oceans and sea ice with synthetic-aperture radar. *JPL pub.* 81-120, NASA Jet Propulsion Laboratory.
- FULTON, R., ZRNIC, D. S. & DOVIK, R. J. 1990 Initiation of a solitary wave family in the demise of a nocturnal thunderstorm density current. *J. Atmos. Sci.* **47**, 319–337.
- GEAR, J. & GRIMSHAW, R. 1983 A second order theory for solitary waves in shallow fluids. *Phys. Fluids* **26**, 14–29.
- HORN, D. A., REDEKOPP, L. G., IMBERGER, J. & IVEY, G. 2000 Internal wave evolution in a space–time varying field. *J. Fluid Mech.* **424**, 279–301.
- HOSEGOOD, P. & VAN HAREN, H. 2003 Near-bed solibores over the continental slope in the Faeroe–Shetland Channel. *Deep-Sea Res.* **51**, 2943–2971.
- KLYMAK, J. M. & MOUM, J. N. 2003 Internal solitary waves of elevation advancing on a shoaling shelf. *Geophys. Res. Lett.* **34**, 3-1–3-4.
- KUNDU, P. K. 1990 *Fluid Mechanics*. Academic.
- LAMB, K. G. 2003 Shoaling solitary internal waves: on a criterion for the formation of waves with trapped cores. *J. Fluid Mech.* **478**, 81–100.
- LAMB, K. G. & YAN, L. 1996 The evolution of internal wave undular bores: comparisons of a fully nonlinear numerical model with weakly nonlinear theory. *J. Phys. Oceanogr.* **26**, 2712–2734.
- LEE, C. & BEARDSLEY, R. 1974 The generation of lone nonlinear internal waves in a weakly stratified shear flow. *J. Geophys. Res.* **79**, 453–462.
- MASLOWE, S. & REDEKOPP, L. 1980 Long nonlinear waves in stratified shear flows. *J. Fluid Mech.* **101**, 321–348.
- MOUM, J. N., FARMER, D. M., SMYTH, W. D., ARMI, L. & VAGLE, S. 2003 Structure and generation of turbulence at interfaces strained by internal solitary waves propagating shoreward over the continental shelf. *J. Phys. Oceanogr.* **33**, 2093–2112.
- MOUM, J. N., GREGG, M. C., LIEN, R. C. & CARR, M. 1995 Comparison of turbulence kinetic energy dissipation rate estimates from two ocean microstructure profilers. *J. Atmos. Ocean. Technol.* **12**, 346–366.

- MOUM, J. N., KLYMAK, J. M., NASH, J. D. & PERLIN, A. 2005 Nonlinear bottom flows over the continental shelf. *J. Phys. Oceanogr.* *in preparation*. Q2
- PEDLOSKY, J. 2003 *Waves in the Ocean and Atmosphere*. Springer.
- PINKEL, R. 2000 Internal solitary waves in the warm pool of the western equatorial pacific. *J. Phys. Oceanogr.* **30**, 2906–2926.
- ROTTMAN, J. W. & SIMPSON, J. E. 1989 The formation of internal bores in the atmosphere: a laboratory model. *Q. J. R. Met. Soc.* **115**, 941–963.
- SCOTTI, A., BUTMAN, R., BEARDSLEY, R. C., ALEXANDER, P. S. & ANDERSON, S. 2005 A lagged beam-to-earth transformation to measure short-wavelength internal waves with an acoustic Doppler current profiler ADCP. *J. Atmos. Ocean. Technol.* *in press*. Q2
- SMITH, R. K., CROOK, N. & ROFF, G. 1982 The Morning Glory: an extraordinary atmospheric undular bore. *Q. J. R. Met. Soc.* **108**, 937–956.
- ZHAO, Z., KLEMAS, V., ZHENG, Q., LI, K. & YAN, X.-H. 2004 Estimating parameters of a two-layer stratified ocean from polarity conversion of internal solitary waves in satellite SAR images. *Remote Sens. of Environ.* **92**, 276–287.

